



Disentangling the role of bond lengths and orbital symmetries in controlling T_c of optimally doped $\text{YBa}_2\text{Cu}_3\text{O}_7$

Francois Jamet ^{1,*}, Cedric Weber, ^{1,†} Swagata Acharya ^{1,2}, Dimitar Pashov,¹ and Mark van Schilfgaarde^{1,3}

¹King's College London, Theory and Simulation of Condensed Matter, The Strand, WC2R 2LS London, United Kingdom

²Institute for Molecules and Materials, Radboud University, NL-6525 AJ Nijmegen, The Netherlands

³National Renewable Energy Laboratory, Golden, Colorado 80401, USA



(Received 15 January 2021; revised 13 May 2021; accepted 19 April 2022; published 7 September 2022)

Optimally doped $\text{YBa}_2\text{Cu}_3\text{O}_7$ (YBCO) has a high critical temperature, at 92 K. It is largely believed that Cooper pairs form in YBCO and other cuprates because of spin fluctuations, but the issue and the detailed mechanism are far from settled. In the present work, we employ a state-of-the-art first-principles ability to compute both the low- and high-energy spin fluctuations in optimally doped YBCO. We benchmark our results against recent inelastic neutron scattering and resonant inelastic x-ray scattering measurements. Further, we use strain as an external parameter to modulate the spin fluctuations and superconductivity. We disentangle the roles of barium-apical oxygen hybridization, interlayer coupling, and orbital symmetries by applying an idealized strain, and also a strain with a fully relaxed structure. We show that shortening the distance between Cu layers is conducive to enhanced Fermi surface nesting, which increases spin fluctuations and drives up T_c . However, when the structure is fully relaxed, electrons flow to the d_{z^2} orbital as a consequence of a shortened Ba-O bond, which is detrimental for superconductivity.

DOI: [10.1103/PhysRevResearch.4.033189](https://doi.org/10.1103/PhysRevResearch.4.033189)

The origin of superconductivity in cuprates remains highly debated, even though more than three decades have passed since cuprates were discovered. It is largely believed that at least for several variants of cuprates, it is primarily spin fluctuations that drive superconductivity [1,2]. However, the issue is far from settled. It is difficult to resolve because the phase diagram is very dense: small excursions in parameter space drive the material from one phase to a new phase. Multiple low-energy scales are present and sometimes intertwined. Theoretically, the challenge has been to develop a material-specific ability that incorporates all such interactions in the right proportions, which can also predict ways to disentangle their roles. Optimally doped $\text{YBa}_2\text{Cu}_3\text{O}_7$ (YBCO) is one of the higher T_c superconductors in the cuprate family. In this work, we present a high-fidelity first-principles theory that is designed to realize this objective, and we use it to explore how spin fluctuations and superconductivity can be modified through strain. In a recent ultrafast experiment [3] on $\text{YBa}_2\text{Cu}_3\text{O}_7$, large-amplitude distortions on apical oxygens were induced to modulate the interlayer coupling. Here we apply a uniaxial strain along the c -axis. We perform two distinct excursions under strain: (a) an ideal strain where all atoms displace in proportion to their height along the c axis,

and (b) allowing the internal coordinates to relax under the strain. We show that strain modifies superconductivity in both cases, but in different ways, thus highlighting how a detailed understanding of the mechanism is essential in order to predict and control unconventional superconductivity.

High-resolution inelastic neutron scattering (INS) data for spin fluctuations exist [4,5], but the data are available only up to 60 meV. State-of-the-art recent resonant inelastic x-ray scattering (RIXS) picks up the signatures of bosonic fluctuations of different kinds [6–8], including those whose mechanisms are intertwined. Thus to decipher what constitutes the primary component of the observed RIXS spectra is a challenge for both theorists and experimentalists alike. RIXS data have been taken from the Cu- L_3 edge for $\text{YBa}_2\text{Cu}_3\text{O}_7$ along the $(0,\pi)$ line [6] with excitations observed up to 300 meV. However, measurements could not be performed for the important momentum region around (π, π) , which likely drives superconductivity.

In the present paper, we calculate the magnetic susceptibilities and superconducting instability for optimally doped YBCO (stoichiometric phase) using a new high-fidelity, first-principles approach [9,10]. We note, however, that the electron-phonon interaction is not included in this framework. For the one-particle Green's function, it combines the quasiparticle self-consistent GW (QS GW) approximation [11] with CTQMC solver [12] based dynamical mean-field theory (DMFT). This framework [13,14] is extended by computing the local vertex from the two-particle Green's function by DMFT [15,16], which is combined with nonlocal bubble diagrams to construct a Bethe-Salpeter equation [17,18]. The latter is solved to yield the essential two-particle spin and charge susceptibilities χ^d and χ^m —physical observables that

*francois.jamet@kcl.ac.uk

†cedric.weber@kcl.ac.uk

provide an important benchmark. Moreover, they supply ingredients needed for the Eliashberg equation, which yields eigenvalues and eigenfunctions that describe instabilities to superconductivity. We will denote QSGW⁺⁺ as a shorthand for the four-tier QSGW+DMFT+BSE+Eliashberg theory. The numerical implementation is discussed in Ref. [10], and codes are available on the open-source electron structure suite Questaal [19]. Some details are also given in Appendix.

QSGW⁺⁺ has high fidelity because QSGW captures nonlocal dynamic correlation particularly well in the charge channel [10,20], but it cannot adequately capture the effects of spin fluctuations. DMFT does an excellent job at the latter, which are strong but mostly controlled by a local effective interaction given by U and J . In this paper, we have used $U = 8$ eV and $J = 0.7$ eV, which is similar to what is generally used for cuprates [21]. That it can well describe superconductivity has now been established in several materials [17,18].

In YBCO, we explore the full potential of our ability by performing rigorous benchmarking of our computed magnetic susceptibilities (resolved in momentum and energy) against the low- and high-energy spectral data from INS and RIXS, respectively. We show that we reproduce most of the intricate structures in momentum and energy spaces observed in INS and RIXS from our theory. That it is possible to reproduce the RIXS spectra from the spin susceptibility alone indicates that RIXS is measuring an excitation that is primarily magnetic in nature in this compound.

The superconducting glue that the present theory can characterize originates from some combination of spin and charge susceptibility [15,17]. That we are able to reliably recover experimental neutron and RIXS data provides some confirmation that we have an adequate foundation to describe superconductivity of this kind. We can use the same method to probe how spin fluctuations and superconductivity are affected when the system is perturbed, in particular how T_c evolves with tensile strain. In a prior work [17], this machinery was used to explain in detail how T_c evolves with tensile strain in Sr₂RuO₄, where it could be benchmarked against experiments.

Figure 1 benchmarks the dynamical structure factor $S(q, \omega) = (1 - e^{-\beta\omega})^{-1} \text{Im} \chi^{\text{mag}}(q, \omega)$ computed by QSGW⁺⁺ [Fig. 1(b)] against direct INS measurements of S [Fig. 1(a)] in the vicinity of the antiferromagnetic point $Q_{\text{AF}} = (\pi, \pi)$, and also against RIXS, which measures any bosonic excitation, including the magnetic structure factor [Fig. 1(c)]. For the former, we can compare only up to maximum value reported, 60 meV. Up to 40 meV, QSGW⁺⁺ is in good qualitative agreement. We note that the features appearing between 40 and 60 meV are not captured; however, these features are an order of magnitude smaller than the main feature, which makes them difficult to capture due to the analytical continuation procedure using the maximum entropy method [22]. Since the RIXS measurement [8] did not sample the region close to Q_{AF} , we compare to RIXS along the line Q connecting Γ and $(\pi, 0)$. A second branch appears at high energy. For both low-energy and high-energy excitations, the maxima of the peaks along the Q line shown by the dashed line are in very good agreement with the experimental data (blue dots). It shows that the measured magnetic RIXS response has peaks at the same energies as

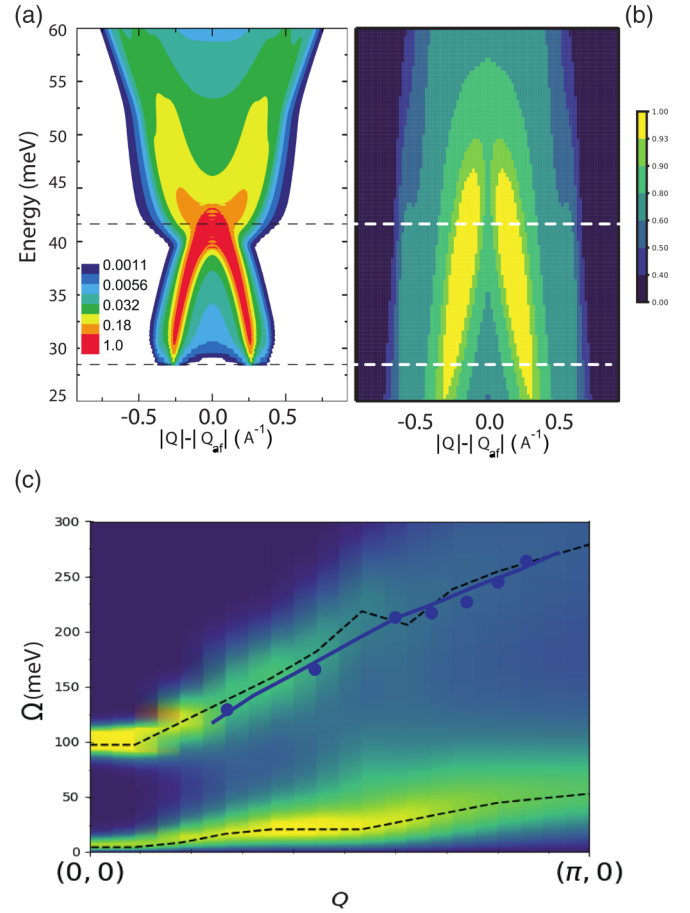


FIG. 1. (a) Structure factor obtained by inelastic neutron scattering along the nodal line obtained at $T = 10$ K in the superconducting phase, reproduced from [4]. (b) Structure factor for the same energy window obtained by QSGW⁺⁺ in the paramagnetic phase. (c) Heat map representing the dynamical structure factor along the path $(0,0)$ - $(\pi, 0)$ in the Brillouin zone computed with QSGW⁺⁺. The dashed line indicates the position of the maxima. Circles denote RIXS experimental data shown for comparison, reproduced from [8] [Fig. 3(b)].

the computed magnetic susceptibility, which further supports that the theoretical magnetic susceptibility is a good model for the magnetic RIXS response, which has been a controversial assumption [23–25].

Next we use the Eliashberg theory derived from spin and charge susceptibilities to estimate T_c , and we investigate how it is affected by strain. We use QSGW⁺⁺ to simulate a uniaxial strain on the c -direction, and we study its effect on the superconducting order. The uniaxial strain is carried out by reducing the c -axis up to 8% with a concomitant expansion of the plane. The volume change $\frac{\Delta V}{V}$ and the reduction of c are related by $\frac{\Delta V}{V} = (1 - 2\nu)\frac{\Delta c}{c}$, where the Poisson ratio used is $\nu = 0.25$, which is close to experiment [26]. For each strain, we consider two scenarios: an ideal strain where all internal displacements are fixed to their projection along the c axis, and another case in which atoms are relaxed to the zero-force condition. Forces are computed within density functional theory. We will denote these scenarios as SS (for single shot) and SO (for structure optimized). SO corresponds to the actual mechanical response of YBCO subject to an ϵ_{33} tensile strain.

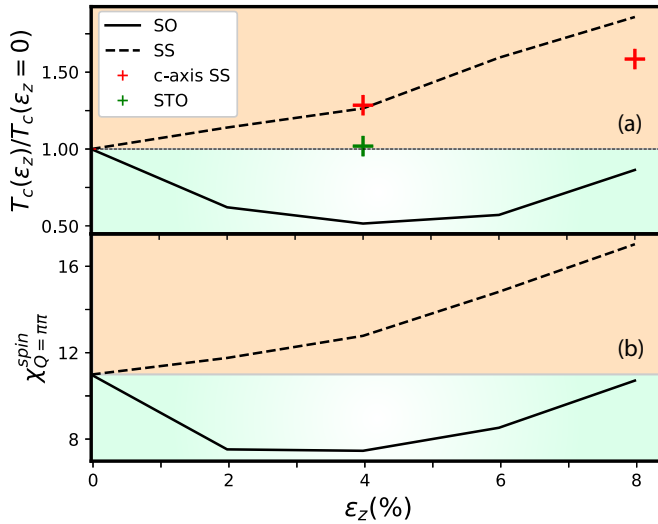


FIG. 2. Top panel: T_c relative to the unstrained condition for the SS case (dashed line) and the SO case (solid line). T_c increases in the former case but decreases in the latter (see the text). The red crosses show the SS case assuming a Poisson ratio of 0 (the basal plane is kept frozen). This shows that the dominant effect is the change in coupling along the c axis. The green cross corresponds to a compression of 2% in the basal plane in the SS case. Panel (b) shows the corresponding evolution of the static magnetic susceptibility at $Q = (\pi, \pi)$. Its close correspondence with T_c indicates that spin fluctuations are the dominant contributor to the superconducting instability.

For convenience of presentation, we define a strain with the opposite sign of the usual definition: $\epsilon_z = -\epsilon_{33} = \frac{c_0 - c}{c_0}$.

For both scenarios, we compute the variation of the critical temperature T_c by comparing the superconducting instability computed by solving the linearized Eliashberg equation (see Appendix). Comparing these two scenarios distinguishes two competing effects: on the one hand, the ideal strain changes the topology of the Fermi surface in a way that favors superconducting order. On the other hand, subsequently allowing the internal coordinates to fully relax empties the d_{z^2} orbital, which is unfavorable for the superconducting order.

Figure 2 shows these results in more detail. T_c is greatly increased in the SS scenario, and the middle and bottom panels show how T_c is correlative to magnetic susceptibility at (π, π) . Both the spin fluctuation and the superconductivity instability show a similar trend, which confirms that the spin fluctuations are an essential contributor of the superconductivity. We can also separate the contributions from stretching the c axis from the contributions made by reductions in the basal plane by varying the Poisson ratio. In one case we used $\nu = 0$, which freezes the lattice vector in the basal plane (red symbols in Fig. 2). T_c changes only marginally with ν , which indicate that the main effects are coming from the reduction of the c -axis. In another scenario, we expand a and b axes about 2% to match $\text{YBa}_2\text{Cu}_3\text{O}_7$ epitaxially on an STO substrate [27] (green symbol). We note, however, that growing perovskite thin films on oxide substrates brings in a breadth of interesting phenomena, such as oxygen octahedral rotations that correlate with magnetism (see, for instance, Ref. [28]), and likely with changes in T_c ultimately. As the main focus of this work is

TABLE I. Interlayer Cu-Cu spacing (first column), copper to apical oxygen distance (second column), and vertical component of AO to Ba distance (third column). We report distances for the pristine material (first row) and under uniaxial strain (ϵ_z). Parameters for ideal (SS) and fully relaxed (SO) structures are shown.

ϵ_z (%)	Cu ¹ -Cu ² (Å)		Cu-AO (Å)		Ba-AO (Å)	
	SO	SS	SO	SS	SO	SS
0.0	3.39	3.39	2.30	2.30	0.30	0.30
4.0	3.32	3.28	2.15	2.22	0.22	0.29
8.0	3.15	3.16	2.08	2.15	0.21	0.28

identifying key underlying mechanisms for changes of T_c , we have not systematically studied the effect of epitaxial strain. Moreover, we go beyond the typical strain values accessible in experiment.

On the $(0, 0)$ - (π, π) line, the Cu $d_{x^2-y^2}$ in the two planes of $\text{YBa}_2\text{Cu}_3\text{O}_7$ couple weakly through the apical O, splitting these otherwise degenerate states into a bond-antibond pair. The Fermi surface connected with these orbitals splits into two sheets.

As shown in Fig. 3, the Fermi surface is formed of three bands. The two curved lines correspond to the bonding and antibonding $d_{x^2-y^2}$ bands noted above. The interlayer hybridization is strongest at the two antinodal points where either $Q_x = \pi$ or $Q_y = \pi$. As strain is applied, the interlayer distance decreases (see Table I). This increases the interlayer hybridization, which further splits the bonding and antibonding $d_{x^2-y^2}$ Fermi surfaces. The antibonding surface becomes flatter and thus more square. Making the arc more square improves the nesting of momentum transfer $Q = (\pi, \pi)$ for electrons living at the antinodal point. In d -wave superconductivity it increases the attractive interaction [29,30], i.e., it works constructively for d -wave superconductivity. As shown in Fig. 4, not only does the magnetic susceptibility increase but the nesting vector moves closer to Q_{AF} , where the magnetic susceptibility is maximum. These two effects cumulatively explain the large enhancement of T_c observed in the SS scenario.

In the SO scenario, we observe a similar splitting of the bonding and antibonding $d_{x^2-y^2}$ Fermi surfaces, but with an important difference. In the SO case, the $d_{x^2-y^2}$ hybridize with d_{z^2} . This hybridization increases because relaxation reduces the Ba-AO vertical distance, e.g., by 25% when the c -axis is reduced by 4% (see Table I). As a consequence, the AO environment is changed, which affects the Cu d_{z^2} orbital. In the unstrained case, d_{z^2} sits at -1.48 eV below the Fermi level, and it is marginally changed in the SS case (for $\epsilon_z = 4\%$ it resides at -1.41 eV) while in the SO case d_{z^2} is pushed closer to the Fermi level (-1.18 eV). The Fermi surface mainly composed of the $d_{x^2-y^2}$ state becomes strongly hybridized with d_{z^2} . This is apparent from the color bar in Fig. 3. The two orbitals hybridize close to the antinodal point, which is known to be unfavorable to d -wave superconductivity [31–33]. Indeed, not only is d_{z^2} unfavorable for T_c , but the opposite-spin nearest-neighbor coupling to form a Cooper pair is less favorable when two orbitals are active at the Fermi level. When d_{z^2}

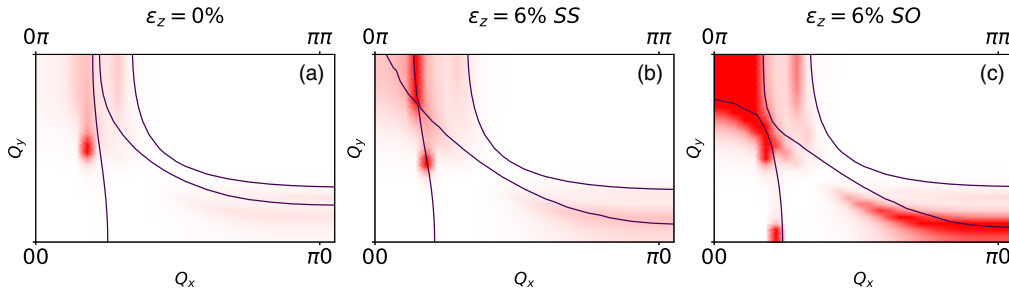


FIG. 3. Evolution of the Fermi surface against applied strain, as computed from QSGW⁺⁺. The Fermi surface (full lines) is composed of a vertical line originating from the CuO chain, and other are lines from the bilayer coupling as explained in the text. Strain increases the separation between antibonding and bonding Fermi sheets for both (a) ideal strain (SS) and (b) fully relaxed strain (SO). SS and SO differ in the degree in which $d_{x^2-y^2}$ and d_{z^2} are coupled, as discussed in the text. This is manifest by the color bar, which shows the off-diagonal component $|G(Q, \omega=0)_{z^2, x^2-y^2}|$, an indicator of the hybridization between d_{z^2} and $d_{x^2-y^2}$ on the Fermi surface.

orbitals are not included in correlated subspace and in the Eliashberg equation, this destructive effect disappears.

To recap, in the idealized scenario compression of the planes increases the interlayer hybridization, which enhances Fermi surface nesting and hence T_c . However, with a proper relaxation (SO), the Ba-AO bond length decreases dramatically to force out-of-plane contributions to the planar physics, and it changes the orbital components of the Fermi surface. This contribution works destructively for T_c .

To conclude, we have first shown that QSGW⁺⁺ is able to predict magnetic fluctuations in YBa₂Cu₃O₇ with high fidelity. Using this technique to explore the parameter space when YBa₂Cu₃O₇ is subject to strain, we find that T_c can be dramatically altered, but how it is altered depends on the details of the displacements. Subject to an ideal strain with no internal relaxation, T_c is increased due to enhanced interlayer hybridization, which changes the shape of the Fermi surface and makes nesting more favorable. However, in a more realistic scenario, the Fermi surface also suffers from a competing d_{z^2} hybridization, which is detrimental to T_c .

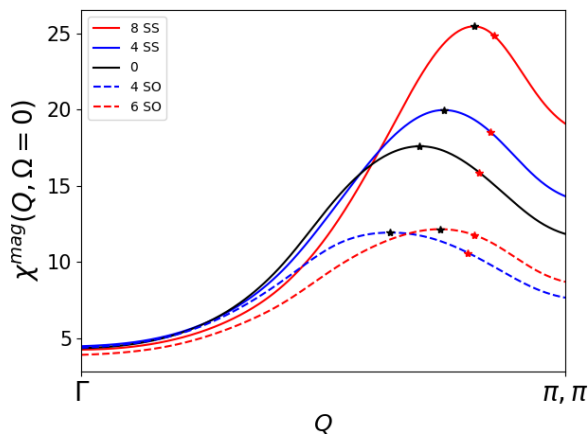


FIG. 4. Static magnetic susceptibility $\chi(q, \omega=0)$ on the $(0,0)$ - (π, π) line for pristine YBCO (black line) and YBCO subject to SS and SO kinds of strain. SS and SO induce opposite effects on both the peak position and the amplitude $\chi(q, \omega=0)$. In the SS case, T_c increase both because $\chi(q, \omega=0)$ increases and the peak shifts closer to Q_{AF} .

C.W. acknowledges insightful and stimulating discussions with Antoine Georges. This work was supported by the Simons Many-Electron Collaboration. C.W. was supported by Grant No. EP/R02992X/1 from the UK Engineering and Physical Sciences Research Council (EPSRC). F.J. was supported by the EPSRC Centre for Doctoral Training in Cross-Disciplinary Approaches to Non-Equilibrium Systems (CANES, EP/L015854/1), and by the Simons Many-Electron Collaboration. For computational resources, we thank PRACE for granting us access to SuperMUC at GCS@LRZ, Germany and Irene-Rome hosted by TGCC, France and Cambridge Tier-2 system operated by the University of Cambridge Research Computing Service [34] funded by EPSRC Tier-2 capital Grant No. EP/P020259/1 and ARCHER UK National Supercomputing Service.

APPENDIX: METHODOLOGY

The calculation in the unstrained case was performed using crystal structure reported in [35]. For the unstrained case, the internal displacements are kept in fixed proportion of their projection along the c -axis. In the SO case, The atomic positions are relaxed to the zero-force condition. Forces are computed using DFT-LDA. The resulting atomic positions are given in Table I.

Paramagnetic DMFT is combined with nonmagnetic QSGW via local projection on Cu $3d$ on the Cu augmentation spheres to form the correlated subspace. DMFT loop was performed using a CTQMC impurity solver [12,36]. The two-particle susceptibility needed in BSE for the magnetic susceptibility was computed using an exact diagonalization impurity solver with six bath sites on a mesh of 50 bosonic frequencies and 500 fermionic frequencies. A benchmark was done with a CTQMC solver to check the accuracy of the hybridization fit. All DMFT calculations were performed at $\beta = 100 \text{ eV}^{-1}$, and analytical continuation was performed using the maximum entropy method [22].

The Eliashberg equation was solved at $\beta = 100 \text{ eV}^{-1}$ and the magnitude of the superconductivity instability was compared for different pressures. We solve the particle-particle ladder Bethe Salpeter equations (BSEs) in the same orbital basis in which DMFT is performed and the vertex is computed. In this context, the vertex was computed

with a CTQMC solver. Single-site DMFT incorporates local correlations and cannot lead to phase transitions that involve nonlocal interactions. On top of DMFT, when BSEs in different particle-particle and particle-hole channels are solved at high temperatures ($T > T_c$) which are normal to the superconducting phase, they tell us about the temperature-dependent evolution of different two-particle instabilities, but they cannot drive us into an ordered phase. So essentially our approach is an above T_c instability approach. The only approximation

involved in solving the particle-particle ladder BSEs is that we solve them for uniform ($\mathbf{q} = \mathbf{0}$) and static ($\Omega = 0$) superconducting instability. We compute the eigenvalue spectrum by solving them at different temperatures ($T > T_c$) and look for the temperature at which the leading eigenvalue in the superconducting channel can in principle become 1, so that the particle-particle ladder BSE diverges, showing an instability towards superconducting ordering. The entire method is discussed in detail in [15,17,37,38].

-
- [1] T. Dahm, V. Hinkov, S. V. Borisenko, A. A. Kordyuk, V. B. Zabolotnyy, J. Fink, B. Büchner, D. J. Scalapino, W. Hanke, and B. Keimer, Strength of the spin-fluctuation-mediated pairing interaction in a high-temperature superconductor, *Nat. Phys.* **5**, 217 (2009).
- [2] D. J. Scalapino, A common thread: The pairing interaction for unconventional superconductors, *Rev. Mod. Phys.* **84**, 1383 (2012).
- [3] W. Hu, S. Kaiser, D. Nicoletti, C. R. Hunt, I. Gierz, M. C. Hoffmann, M. Le Tacon, T. Loew, B. Keimer, and A. Cavalleri, Optically enhanced coherent transport in $\text{YBa}_2\text{Cu}_3\text{O}_{6.5}$ by ultrafast redistribution of interlayer coupling, *Nat. Mater.* **13**, 705 (2014).
- [4] D. Reznik, J.-P. Isern, I. Eremin, L. Pintschovius, T. Wolf, M. Arai, Y. Endoh, T. Masui, and S. Tajima, Local-moment fluctuations in the optimally doped high- T_c superconductor $\text{YBa}_2\text{Cu}_3\text{O}_{6.95}$, *Phys. Rev. B* **78**, 132503 (2008).
- [5] H. Woo, P. Dai, S. M. Hayden, H. A. Mook, T. Dahm, D. J. Scalapino, T. Perring, and F. Doğan, Magnetic energy change available to superconducting condensation in optimally doped $\text{YBa}_2\text{Cu}_3\text{O}_{6.95}$, *Nat. Phys.* **2**, 600 (2006).
- [6] L. J. P. Ament, M. van Veenendaal, T. P. Devereaux, J. P. Hill, and J. van den Brink, Resonant inelastic x-ray scattering studies of elementary excitations, *Rev. Mod. Phys.* **83**, 705 (2011).
- [7] M. Hepting, L. Chaix, E. W. Huang, R. Fumagalli, Y. Y. Peng, B. Moritz, K. Kummer, N. B. Brookes, W. C. Lee, M. Hashimoto, T. Sarkar, J.-F. He, C. R. Rotundu, Y. S. Lee, R. L. Greene, L. Braicovich, G. Ghiringhelli, Z. X. Shen, T. P. Devereaux, and W. S. Lee, Three-dimensional collective charge excitations in electron-doped copper oxide superconductors, *Nature* **563**, 374 (2018).
- [8] M. Le Tacon, G. Ghiringhelli, J. Chaloupka, M. M. Sala, V. Hinkov, M. W. Haverkort, M. Minola, M. Bakr, K. J. Zhou, S. Blanco-Canosa, *et al.*, Intense paramagnon excitations in a large family of high-temperature superconductors, *Nat. Phys.* **7**, 725 (2011).
- [9] L. Sponza, P. Pisanti, A. Vishina, D. Pashov, C. Weber, M. van Schilfgarde, S. Acharya, J. Vidal, and G. Kotliar, Self-energies in itinerant magnets: A focus on Fe and Ni, *Phys. Rev. B* **95**, 041112(R) (2017).
- [10] D. Pashov, S. Acharya, R. L. W. Lambrecht, J. Jackson, K. D. Belashchenko, A. Chantis, F. Jamet, and M. van Schilfgarde, Questaal: A package of electronic structure methods based on the linear muffin-tin orbital technique, *Comput. Phys. Commun.* **249**, 107065 (2020).
- [11] T. Kotani, M. van Schilfgarde, and S. V. Faleev, Quasiparticle self-consistent gw method: A basis for the independent-particle approximation, *Phys. Rev. B* **76**, 165106 (2007).
- [12] K. Haule, Quantum monte carlo impurity solver for cluster dynamical mean-field theory and electronic structure calculations with adjustable cluster base, *Phys. Rev. B* **75**, 155113 (2007).
- [13] S. Acharya, C. Weber, E. Plekhanov, D. Pashov, A. Taraphder, and M. van Schilfgarde, Metal-Insulator Transition in Copper Oxides Induced by Apex Displacements, *Phys. Rev. X* **8**, 021038 (2018).
- [14] E. Baldiniand *et al.*, Electron-phonon-driven three-dimensional metallicity in an insulating cuprate, *Proc. Natl. Acad. Sci. (USA)* **117**, 6409 (2020).
- [15] H. Park, The study of two-particle response functions in strongly correlated electron systems within the dynamical mean field theory, Ph.D. thesis, Rutgers University-Graduate School-New Brunswick (2011).
- [16] Z. Yin, K. Haule, and G. Kotliar, Spin dynamics and orbital-antiphase pairing symmetry in iron-based superconductors, *Nat. Phys.* **10**, 845 (2014).
- [17] S. Acharya, D. Pashov, C. Weber, H. Park, L. Sponza, and M. van Schilfgarde, Evening out the spin and charge parity to increase T_c in Sr_2RuO_4 , *Commun. Phys.* **2**, 163 (2019).
- [18] S. Acharya, D. Pashov, F. Jamet, and M. van Schilfgarde, Controlling t_c through Band Structure and Correlation Engineering in Collapsed and Uncollapsed Phases of Iron Arsenides, *Phys. Rev. Lett.* **124**, 237001 (2020).
- [19] Questaal website, <https://www.questaal.org>.
- [20] J. Tomczak, P. Liu, A. Toschi, G. Kresse, and K. Held, Merging GW with DMFT and non-local correlations beyond, *Eur. Phys. J.: Spec. Top.* **226**, 2565 (2017).
- [21] S. Choi, A. Kutepov, K. Haule, M. van Schilfgarde, and G. Kotliar, First-principles treatment of mott insulators: Linearized QSGW + DMFT approach, *npj Quantum Mater.* **1**, 16001 (2016).
- [22] D. Bergeron and A. M. S. Tremblay, Algorithms for optimized maximum entropy and diagnostic tools for analytic continuation, *Phys. Rev. E* **94**, 023303 (2016).
- [23] D. Benjamin, I. Klich, and E. Demler, Single-band Model of Resonant Inelastic X-ray Scattering by Quasiparticles in High- T_c Cuprate Superconductors, *Phys. Rev. Lett.* **112**, 247002 (2014).
- [24] M. Minola, G. Dellea, H. Gretarsson, Y. Peng, Y. Lu, J. Porras, T. Loew, F. Yakhov, N. Brookes, Y. Huang, *et al.*, Collective Nature of Spin Excitations in Superconducting Cuprates Probed by Resonant Inelastic X-Ray Scattering, *Phys. Rev. Lett.* **114**, 217003 (2015).
- [25] M. Kanász-Nagy, Y. Shi, I. Klich, and E. A. Demler, Resonant inelastic x-ray scattering as a probe of band

- structure effects in cuprates, *Phys. Rev. B* **94**, 165127 (2016).
- [26] C. Chen, L. Liu, Y. Wen, Y. Jiang, and L. Chen, Elastic properties of orthorhombic $\text{YBa}_2\text{Cu}_3\text{O}_7$ under pressure, *Crystals* **9**, 497 (2019).
- [27] H. Y. Zhai and W. K. Chu, Effect of interfacial strain on critical temperature of $\text{YBa}_2\text{Cu}_3\text{O}_{7-\delta}$ thin films, *Appl. Phys. Lett.* **76**, 3469 (2000).
- [28] X. Zhai, L. Cheng, Y. Liu, C. M. Schlepütz, S. Dong, H. Li, X. Zhang, S. Chu, L. Zheng, J. Zhang, A. Zhao, H. Hong, A. Bhattacharya, J. N. Eckstein, and C. Zeng, Correlating interfacial octahedral rotations with magnetism in $(\text{LaMnO}_{3+\delta})_N/(\text{SrTiO}_3)_N$ superlattices, *Nat. Commun.* **5**, 4283 (2014).
- [29] N. Bickers, D. Scalapino, and R. Scalettar, Cdw and sdw mediated pairing interactions, *Int. J. Mod. Phys. B* **01**, 687 (1987).
- [30] C. Weber, C. Yee, K. Haule, and G. Kotliar, Scaling of the transition temperature of hole-doped cuprate superconductors with the charge-transfer energy, *Europhys. Lett.* **100**, 37001 (2012).
- [31] H. Sakakibara, H. Usui, K. Kuroki, R. Arita, and H. Aoki, Origin of the material dependence of T_c in the single-layered cuprates, *Phys. Rev. B* **85**, 064501 (2012).
- [32] C. E. Matt, D. Sutter, A. M. Cook, Y. Sassa, M. Månsson, O. Tjernberg, L. Das, M. Horio, D. Destraz, C. G. Fatuzzo, *et al.*, Direct observation of orbital hybridisation in a cuprate superconductor, *Nat. Commun.* **9**, 972 (2018).
- [33] H. Sakakibara, H. Usui, K. Kuroki, R. Arita, and H. Aoki, Two-Orbital Model Explains the Higher Transition Temperature of the Single-Layer Hg-Cuprate Superconductor Compared to That of the La-Cuprate Superconductor, *Phys. Rev. Lett.* **105**, 057003 (2010).
- [34] www.hpc.cam.ac.uk.
- [35] J. D. Jorgensen, B. W. Veal, A. P. Paulikas, L. J. Nowicki, G. W. Crabtree, H. Claus, and W. K. Kwok, Structural properties of oxygen-deficient $\text{YBa}_2\text{Cu}_3\text{O}_{7-\delta}$, *Phys. Rev. B* **41**, 1863 (1990).
- [36] P. Seth, I. Krivenko, M. Ferrero, and O. Parcollet, TRIQS/CTHYB: A continuous-time quantum monte carlo hybridisation expansion solver for quantum impurity problems, *Comput. Phys. Commun.* **200**, 274 (2016).
- [37] S. Acharya, D. Pashov, F. Jamet, and M. van Schilfgaarde, Electronic origin of T_c in bulk and monolayer FeSe, *Symmetry* **13**, 169 (2021).
- [38] S. Acharya, D. Pashov, and M. van Schilfgaarde, Role of nematicity in controlling spin fluctuations and superconducting T_c in bulk FeSe, *Phys. Rev. B* **105**, 144507 (2022).